Infinite Science
Publishing

Research Article

Numerical Simulations of 3D Rotational Drift

Anna Vilter · Martin A. Rückert · Thomas Kampf · Volker J. F. Sturm · Volker C. Behr*

University of Würzburg, Experimental Physics V, Würzburg, Germany
*Corresponding author, email: behr@physik.uni-wuerzburg.de

Abstract

Due to its broad range of applications in biology and medicine, detection of magnetic particles gains increasing importance. The established method of magnetic particle imaging (MPI) bases on the non-linear magnetization behavior of superparamagnetic nanoparticles [1]. As an alternative approach, rotational drift spectroscopy (RDS) [2, 3] aims at detecting the properties of magnetic particles in liquid suspensions based on their motional behavior inside an external rotating magnetic field. Serving as basis for the physical understanding and further development of RDS, the rotational behavior of particles with and without motional restriction is studied by numerical simulation. For this purpose, two different approaches were implemented: one using an explicit Euler algorithm and an improved version using a semi-analytical two-step procedure in order to overcome numerical instabilities of the original code. The results show independently of motional restriction two characteristic types of rotational behavior. The particles either follow the external field with a locked phase lag or exhibit a rotational drift.

I. Introduction

In comparison with nuclear magnetic resonance (NMR), which only allows indirect detection of magnetic particles via a negative contrast, magnetic particle imaging (MPI) [1] enables a direct detection. This offers advantages concerning sensitivity as well as specificity. Developed as an alternative to the originally proposed MPI, rotational drift spectroscopy (RDS) [2, 3] also aims at directly detecting magnetic particles in liquid suspension. A focus herein is the examination of particle- and environmental properties, for which RDS offers potential for specifically high sensitivity. Using functionalized particles, this opens a path to bio-sensing applications. Thus primarily conceived as a spectroscopic modality, there are also concepts on how to extend it towards an imaging method [4].

While MPI is based on the non-linear magnetization behavior of superparamagnetic nanoparticles, the concept of RDS is based on the rotational drift of magnetic particles in liquid suspensions. The optical detection of the rotational behavior of individual micro-particles driven by an external magnetic field $\mathbf{B}$ has been previously published [5]. In that publication $\mathbf{B}$ rotates in a plane (hereafter referred to as xy-plane) with constant amplitude B and frequency ω_0. Due to constraints imposed by the experimental setup, the motion of particles was restricted to the xy-plane (hereafter referred to as 2D system). Depending on the ratio $\beta = \Omega_c \omega_0^{-1}$ of the driving frequency ω_0 and a critical frequency $\Omega_c = mB\zeta^{-1}$ two different types of rotational behavior were observed. In the expression for Ω_c, m describes the amplitude of the magnetic moment $\mathbf{m}$ of the particle and the friction coefficient $\zeta = \eta\kappa V$ includes the shape factor κ and the particle volume V as well as the dynamic viscosity η of the surrounding fluid.

For $\beta \geq 1$ the magnetization vector of the particle follows the external field with a characteristic phase lag (*lock case*). For $0 < \beta < 1$ the magnetization vector performs a non-linear rotational drift at periodically oscillating angular velocity $\Omega[t]$ and period of oscillation T (*drift case*). The average angular velocity $\overline{\Omega} = 2\pi T^{-1}$ in

this drift case is given by [5]

$$\overline{\Omega} = \omega_0 - \sqrt{\omega_0 - \Omega_c^2} \qquad \text{for} \qquad \omega_0 > \Omega_c \qquad (1)$$

only depending on parameters of the external field and the observed system (particles and environment). Therefore, it is a characteristic of the system under observation - comparable to the Larmor frequency in magnetic resonance.

RDS aims at measuring inductively the behavior of magnetic particle ensembles as well as their interaction with their environment based on the effect of rotational drift. Thus, for further developments of the RDS concept, mathematical description and simulation of this effect including systems with no motional restriction to the plane of the external field (3D systems) is fundamental and investigated in more detail within this work.

II. Material and Methods

In contrast to the description of the magnetization behavior of SPIOs based on the Langevin theory of paramagnetism, the dynamics of the particles considered in [5] can be described by the time evolution of a magnetic moment $\boldsymbol{m}$. This moment is assumed to be locked relatively to the particle geometry and has a time constant amplitude m. The corresponding equation of motion is given by [6] (neglecting white noise driving torque):

$$\frac{\mathrm{d}\boldsymbol{m}}{\mathrm{d}t} = \frac{1}{\zeta}(\boldsymbol{m} \times \boldsymbol{B}) \times \boldsymbol{m}. \qquad (2)$$

For further considerations, $\boldsymbol{B}$ was chosen as a vector rotating in the xy-plane with time constant angular velocity and amplitude following the assumptions in [5].

First numerical RDS simulations [7] based on an explicit Euler method and thus discretization of Eq. (2):

$$\boldsymbol{m}[t_{i+1}] = \boldsymbol{m}[t_i] + \frac{1}{\zeta}(\boldsymbol{m}[t_i] \times \boldsymbol{B}[t_i]) \times \boldsymbol{m}[t_i]\Delta t. \qquad (3)$$

A successive normalization step of m is required to account for the conservation of the amplitude m.

To resolve issues resulting from this algorithm, an additional semi-analytical two-step procedure was implemented. For this, it was advantageous to change the frame of reference in the following to a coordinate system rotating with $\boldsymbol{B}$ as shown in [8]. In this rotating frame of reference the orthonormal unit vectors $\{\hat{\mathrm{e}}_x, \hat{\mathrm{e}}_y, \hat{\mathrm{e}}_z\}$ are chosen to have $\hat{\mathrm{e}}_x$ in parallel to $\boldsymbol{B}$ and $\hat{\mathrm{e}}_z$ in parallel to its axis of rotation. With that Eq. (2) transforms to

$$\left(\frac{\mathrm{d}\boldsymbol{m}}{\mathrm{d}t}\right)_r = \boldsymbol{\Omega}_r \times \boldsymbol{m} \qquad (4)$$

with substitution

$$\boldsymbol{\Omega}_r[t] = \Omega_c(\hat{\mathrm{n}}_m[t] \times \hat{\mathrm{e}}_x) - \omega_0\hat{\mathrm{e}}_z. \qquad (5)$$

Eq. (4) describes a rotation of $\boldsymbol{m}$ around a current axis of rotation $\boldsymbol{\Omega}_r[t]$ (depending on the current orientation $\hat{\mathrm{n}}[t]$ of $\boldsymbol{m}$ with $\boldsymbol{m}[t] = m\hat{\mathrm{n}}_m[t]$), while the amplitude $\Omega_r[t]$ corresponds to the current angular velocity of $\boldsymbol{m}$ in the rotating frame of reference. This fact is used by the numerical two-step procedure. In the first step, the current axis $\boldsymbol{\Omega}_r[t_i] = \Omega_r[t_i]\hat{\mathrm{n}}_{\Omega_r}[t_i]$ (according to Eq. (5)) and angle of rotation $\Delta\vartheta[t_i] = \Omega_r[t_i]\Delta t$ are calculated. In the second step, the rotation of $\boldsymbol{m}$ around this current axis is executed by using a rotation matrix $\boldsymbol{R}$:

$$\boldsymbol{m}[t_{i+1}] = \boldsymbol{R}\left[\hat{\mathrm{n}}_{\Omega_r}[t_i], \Delta\vartheta[t_i]\right]\boldsymbol{m}[t_i]. \qquad (6)$$

This second algorithm is norm conserving and requires no renormalization as the explicit Euler method.

All data presented in subsection III.I result from numerical simulations based on this two-step procedure. The numbers $\#_{T_0}$ of periods T_0 of the external field $\boldsymbol{B}$ was chosen depending on the questions under investigation, ranging from $\#_{T_0} = 10$ to $\#_{T_0} = 100$. The corresponding number of time steps Δt per period T_0 was chosen to $\#_{\Delta t/T_0} = \Delta t/T_0 = 1 \cdot 10^3$, which provides reasonable numerical results as shown below. To investigate the influence of parameters of the observed system, the simulations were performed for various values of β. The influence of the starting position $\hat{\mathrm{n}}_m[0]$ was analyzed by choosing sets with different numbers $\#_{\hat{\mathrm{n}}_m[0]}$ of normalized magnetization vectors. The orientations were chosen - independent and identically distributed - on a surface of a sphere using an algorithm following [9].

III. Results and Discussion

III.I. Rotational behavior

To obtain better understanding of rotational behavior of 3D systems, initially the time evolution of $\boldsymbol{m}$ was simulated for different starting orientations $\hat{\mathrm{n}}_m[0]$ for $\beta < 1$ (49 orientations) as well as $\beta \geq 1$ (51 orientations) (two-step procedure; simulation parameters: $\#_{T_0} = 10$, $\#_{\Delta t/T_0} = 1 \cdot 10^3$, $\#_{\hat{\mathrm{n}}_m[0]} = 1000$). The resulting trajectories in the rotating frame of reference are shown in Fig. 1 for two β values and four starting orientations (gray arrows). This includes one starting orientation in the xy-plane (dark gray arrow), which corresponds to the special case of the 2D system. Here, the motion is even for the unrestricted case confined to the xy-plane.

The simulated data shows that, in a similar manner to the behavior of 2D systems, also in 3D two different types of rotational behavior depending on β occur. These can be regarded as a 'strong coupling' of the external drive field with the magnetic moment in the *lock case* ($\beta \geq 1$) and a 'weak coupling' in the *drift case* ($\beta < 1$).

For $\beta \geq 1$ (see Fig. 1a), the magnetization performs a transitional motion towards a steady-state in the xy-plane. Considering the simulated $\hat{\mathrm{n}}_m[t]$ data in spherical coordinates, this corresponds to a transition of the
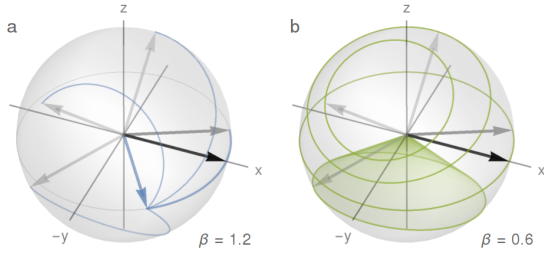
Figure 1: Trajectories of $\boldsymbol{m}$ in the rotating frame: Depending on β, two different types of rotational behavior can be observed. a) *lock case*: For $\beta \geq 1$, the magnetization performs a transitional motion to a β-dependent characteristic position (blue arrow) in the xy-plane (gray circle). b) *drift case*: For $\beta < 1$, the magnetization precesses around a constant rotation axis resulting in circular trajectories.
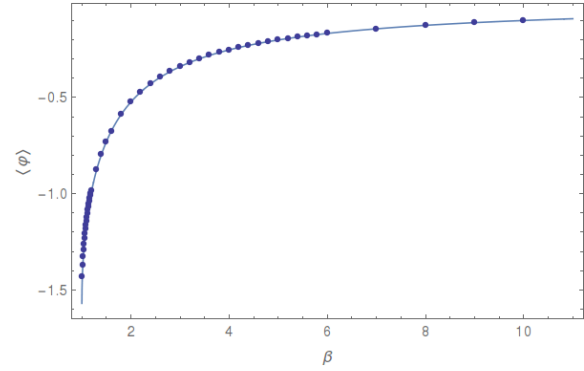

Figure 2: Functional dependency $\varphi[\beta]$ of the resulting time constant phase lag in the xy-plane for $\beta \geq 1$ (dark blue dots: simulated ensemble average $\langle\varphi\rangle$; blue curve: theoretically predicted dependency according to Eq. (7)).

polar angle θ towards $\pi/2$ for all simulated starting orientations $\hat{n}_m[0]$ and β values. Statistical evaluation of this transition shows that for each $\beta > 1$ the standard deviation of all orientations of $\hat{n}_m[t]$ decreases rapidly towards $\text{std}[\theta] = 6.22 \cdot 10^{-15}$ - independently of the original starting orientation. This limit is given by attainable numerical precision. The higher the value of β, the faster this transitional motion takes place. Thus, e.g. for $\beta = 7$ it takes less than one period T_0 of the external field until reaching this final standard deviation, where for $\beta = 1.2$ this transition takes approximately ten periods T_0 and for $\beta = 1.01$ more than $40 T_0$. For each individual value of β all magnetization vectors end up in the same point in the xy-plane. The corresponding azimuth angle $\varphi[\beta]$ matches the characteristic phase lag of the 2D system as shown in Fig. 2. The simulated values depicted in this figure correspond to the ensemble average $\langle\varphi\rangle$ over all starting orientations for each individual β value at the time at which the standard deviation converges as described above. The standard deviation $\text{std}[\theta]$ associated with $\langle\varphi\rangle$ is less than $6 \cdot 10^{-14}$, which again constitutes the attainable numerical precision limit. The theoretically predicted curve bases on the functional dependency in the 2D system [5]

$$\varphi[\beta] = -\arcsin[1/\beta]. \tag{7}$$

The deviation of the simulated data relative to the theoretically prediction in Eq. (7) is less than $4 \cdot 10^{-12}$.

For $\beta < 1$ (see Fig. 1b) the vector of the magnetic moment $\boldsymbol{m}$ performs a precessing motion on a cone (for reasons of clarity only depicted for one starting orientation) resulting in closed circular trajectories. This corresponds to a time-constant specific orientation $\hat{n}_{\Omega_r}[t] = \hat{n}_{\Omega_r}[0] = \hat{n}_{\Omega_r}$ of $\boldsymbol{\Omega}_r$ for all magnetization vectors starting on the same cone. This constancy of $\hat{n}_{\Omega_r}$ can be shown in the simulated data by deriving the angle

$$\Delta \chi_{\Omega_r} = \arccos[\hat{n}_{\Omega_r}[t_i] \cdot \hat{n}_{\Omega_r}[0]] \tag{8}$$

between the starting orientation $\hat{n}_{\Omega_r}[0]$ and the orientation $\hat{n}_{\Omega_r}[t_i]$ at all other simulated times. Statistical evaluation of these resulting angles shows a maximum standard deviation $\text{std}[\cos[\Delta\chi_{\Omega_r}]] < 3 \cdot 10^{-16}$. So, within the attainable numerical precision, no significant change in the orientation of $\boldsymbol{\Omega}_r$ is observed.
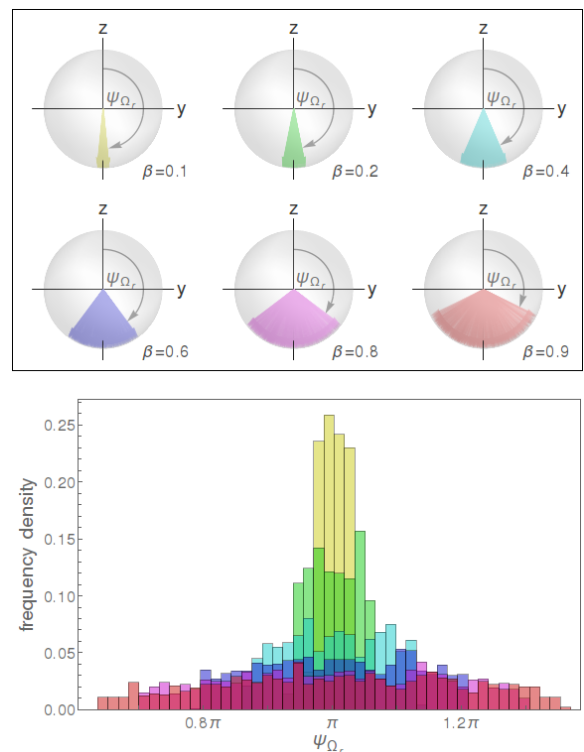

Figure 3: Simulation of the orientation of $\boldsymbol{\Omega}_r$ (two-step procedure; simulation parameters: $\#_{T_0} = 10$, $\#_{\Delta t/T_0} = 1 \cdot 10^3$, $\#_{\hat{n}_m[0]} = 1000$ here shown for $\beta = \{0.1, 0.2, 0.4, 0.6, 0.8, 0.9\}$): resulting distribution of angular coordinates ψ_{Ω_r} depending on β.

However, the respective orientation of $\hat{n}_{\Omega_r}$ depends on β and $\hat{n}_{\Omega_r}[0]$ and has (resulting from cross product with $\hat{e}_x$) no x-component:

$$\hat{n}_{\Omega_r} = \frac{\boldsymbol{\Omega}_r}{|\boldsymbol{\Omega}_r|} = \frac{\beta\left(\hat{n}_{\Omega_r}[0] \times \hat{e}_x\right) - \hat{e}_z}{\left|\beta\left(\hat{n}_{\Omega_r}[0] \times \hat{e}_x\right) - \hat{e}_z\right|}. \tag{9}$$

Therefore, the orientation of $\hat{n}_{\Omega_r}$ can be fully described via the angular coordinate ψ_{Ω_r} in the yz-plane (counting clockwise starting from the z-axis), which shows based on Eq. (9) a characteristic distribution depending on β (see Fig. 3).

As opposed to the orientation of $\boldsymbol{\Omega}_r$ the corresponding amplitude, which equals the angular velocity $\Omega_r[t]$, is not constant over time but oscillates periodically. To examine the average angular velocity $\overline{\Omega}_r$, the period of oscillation $T_r = 2\pi/\overline{\Omega}_r$ was determined for all simulated trajectories (same data as used for the examination of the constancy of $\hat{n}_{\Omega_r}$) via the 2π-periodicity $\vartheta[t_i + T_r] = \vartheta[t_i] + 2\pi$ of the accumulated angle of rotation $\vartheta[t_i] = \sum_n^i \Delta\vartheta[t_n]$. The corresponding error of the determined values thus results from the selected time resolution of the simulation $\Delta t = T_0/\#_{\Delta t/T_0}$. A comparison of all T_r values resulting from the 1000 starting orientations $\hat{n}_{\Omega_r}[0]$ for one defined β value shows a standard deviation $\text{std}[T_r] < 2.5 \cdot 10^{-13}$. Thus, within the attainable numerical precision, all trajectories of one defined β value have the same average angular velocity $\overline{\Omega}_r = 2\pi/T_r$. Therefore, the average angular velocity $\overline{\Omega}_r$ in the rotating frame of reference for 2D systems given according to Eq. (1) also holds true in 3D:

$$\frac{\overline{\Omega}_r}{\omega_0} = \sqrt{1 - \beta^2}. \tag{10}$$
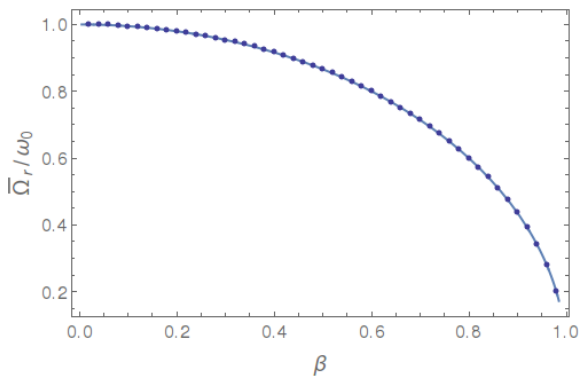
Figure 4: Functional dependency of the average angular velocity $\overline{\Omega}_r[\beta]$ in the rotating frame of reference (dark blue dots: mean values $\langle\overline{\Omega}_r\rangle$ of all trajectories corresponding to one β value; blue curve: theoretical prediction according to Eq. (10)). The simulated and theoretical values are compatible within the range of errors resulting from the time resolution of the simulation.

This functional dependency is plotted in Fig. 4. Therein, the depicted values correspond to the mean values $\langle\overline{\Omega}_r\rangle$ of all trajectories of one β value. They show a maximum deviation of less than 0.03% relative to the theoretically predicted values according to Eq. (9). This is within the range of errors resulting from the time resolution of the simulation.

III.II. Comparison of numerical algorithms

For comparing the implemented numerical algorithms, simulations - with at first identical number of time steps $\#_{\Delta t/T_0}$ - were performed with either algorithm. The resulting trajectories in the rotating frame (in which the orientation $\hat{n}_B$ of the external field $\boldsymbol{B}$ is aligned with the x-axis constant over time) are shown in Fig. 5.
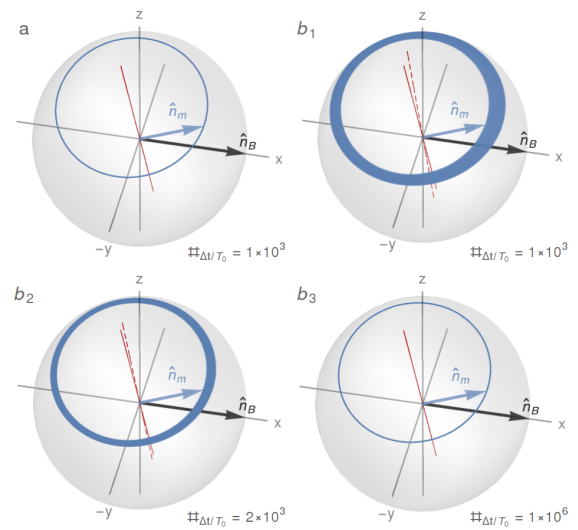
Figure 5: Comparison of the trajectories (blue curves; starting orientation $\hat{n}_m$: blue arrow) in the rotating frame with corresponding axes of rotation (red lines; solid: $t = 0$, dashed: $t = 100\,T_0$) resulting from numerical simulations at different numbers of time steps $\#_{\Delta t/T_0}$. Simulation parameters were: $\#_{T_0} = 100$, $\beta = 0.6$, random starting orientation $\hat{n}_m$ a) two-step procedure b) explicit Euler method. In contrast to the two-step procedure, the explicit Euler method does not provide stable trajectories, which results in an angle $\Delta\chi_{\Omega_r}$ between the axes of rotation over time (cf. parts b1 and b2). The stability can be improved by increasing $\#_{\Delta t/T_0}$.

As shown in the previous subsection for simulations of ten periods T_0, even for $\#_{T_0} = 100$ the data resulting from the two-step procedure describe closed circular trajectories. Furthermore, considering the relative angle $\Delta\chi_{\Omega_r}$ between the actual orientation $\hat{n}_{\Omega_r}[t_i]$ of the axis of rotation for each simulated time step t_i and the starting orientation $\hat{n}_{\Omega_r}[0]$, no significant change in $\Delta\chi_{\Omega_r}$ can be observed $\left(\text{mean}\left[\cos\left[\Delta\chi_{\Omega_r}\right]\right] = 1,\ \text{std}\left[\cos\left[\Delta\chi_{\Omega_r}\right]\right] = 2 \cdot 10^{-16}\right)$.

The data of the explicit Euler method where derived in the laboratory frame according to Eq. (3), but for better

depiction, transformed in the rotating frame. As opposed to the results from the two-step procedure, this algorithm does not provide stable trajectories. This corresponds to an apparent change in the orientation $\hat{n}_{\Omega_r}$ of the axis of rotation: For the simulated data shown in Fig. 5b$_1$, the axis of rotation accumulates an angle $\Delta\chi_{\Omega_r}\left[\#_{\Delta t/T_0} = 1\cdot10^3\right] = 5.1°$ relative to $\hat{n}_{\Omega_r}[0]$ over 100 periods of T_0. Increasing the number of time steps per period reduces this relative angle $\left(\Delta\chi_{\Omega_r}\left[\#_{\Delta t/T_0} = 2\cdot10^3\right] = 2.5°\right)$ and the deviation from the expected circular trajectories (see Fig. 5b$_2$), but even for numbers of time steps three orders of magnitude higher than the numbers of time steps chosen for the two-step procedure (see Fig. 5b$_3$), an increase of $\Delta\chi_{\Omega_r}$ can be observed $\left(\Delta\chi_{\Omega_r}\left[\#_{\Delta t/T_0} = 1\cdot10^6\right] > 16"\right)$. In Fig. 6 the dependency of $\Delta\chi_{\Omega_r}$ as given in Eq. (8) on time is depicted for different values of β. It shows the temporal increase of the error in the explicit Euler method depending on the number of time steps per period. The slight oscillatory behavior of $\Delta\chi_{\Omega_r}$ is caused by the precession of the magnetization around the drifting rotation axis $\mathbf{\Omega}_r$. This causes a periodic change in the drift direction (see Eq. (3) and Eq. (5)) and hence the observed oscillation with the drift frequency Ω_r.
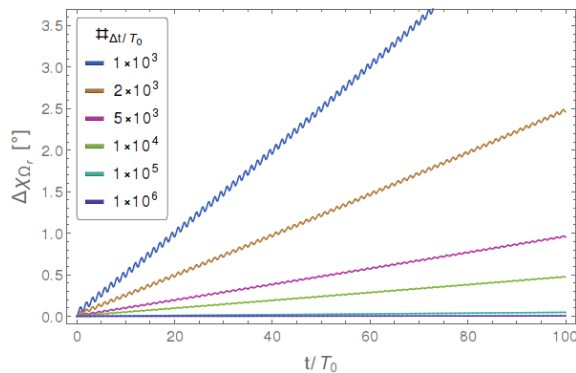

Figure 6: Increase of the relative angle $\Delta\chi_{\Omega_r}$ between $\hat{n}_{\Omega_r}[t_i]$ and $\hat{n}_{\Omega_r}[0]$ (cf. Eq. (8)) of the implemented explicit Euler method (simulation parameters: $\#_{T_0} = 100, \beta = 0.6$, random starting orientation $\hat{n}_m$).

While the two-step procedure reliably yields stable trajectories, the above results show that the easy-to-implement Euler method can also be applied - as long as a sufficiently high number of time steps per period is used to minimize $\Delta\chi_{\Omega_r}$.

IV. Conclusion

RDS requires knowledge about the 3D rotational behavior of magnetic particles in rotating fields, but until now this has only been described for motion restricted to two dimensions. This work shows in numerical simulations that characteristic parameters of the 2D motion - constant phase lag $\varphi[\beta]$ in *lock case* and rotational drift

with an average angular velocity $\overline{\Omega}[\beta]$ in *drift case* - are also exhibited in an unrestricted three dimensional system. Instabilities in the originally employed explicit Euler algorithm are overcome by an improved two-step procedure yielding stable trajectories. The implemented algorithm is easily expandable to study systems of higher complexity including parameter distributions for particles, thermal noise, or more complex field geometries. Especially this expandability and its applicability to arbitrary field geometries are the benefits of the presented numerical solution over an analytical solution that can only cover one specific case. The numerical approach successfully constitutes the essentials of an RDS toolbox that will serve for further simulation of rotational drift behavior to advance RDS.

Acknowledgments

References

[1] B. Gleich and J. Weizenecker. Tomographic imaging using the nonlinear response of magnetic particles. *Nature*, 435(7046):1214–1217, 2005. doi:10.1038/nature03808.

[2] M. Rückert, T. Kampf, and V. Behr. Method for determining the presence of an analyte by means of small magnetic particles, and corresponding device. Patent applications EP000002553455A1, US020130157256A1, WO002011120712A1, filed 2011.

[3] M. A. Rückert, P. Vogel, A. Vilter, W. H. Kullmann, P. M. Jakob, and V. C. Behr. Rotational drift spectroscopy for magnetic particle ensembles. *IEEE Trans. Magn.*, 51(2):6500604, 2015. doi:10.1109/TMAG.2014.2334138.

[4] M. Rückert and V. Behr. Imaging method using magnetic small particles and corresponding device. Patent DE102010013990B4, filed 2010 and patent applications EP000002552310A1, US020130079623A1, WO002011120713A1, filed 2011.

[5] B. H. McNaughton, K. A. Kehbein, J. N. Anker, and R. Kopelman. Sudden breakdown in linear response of a rotationally driven magnetic microparticle and application to physical and chemical microsensing. *J. Phys. Chem. B*, 110(38):18958–18964, 2006. doi:10.1021/jp060139h.

[6] W. T. Coffey, Y. P. Kalmykov, and J. T. Waldron. *The Langevin Equation*. World Scientific, Singapore, 2004.

[7] M. A. Rückert, P. Vogel, T. Kampf, W. H. Kullmann, P. M. Jakob, and V. C. Behr. Simulating the signal generation of rotational drift spectroscopy. *IEEE Trans. Magn.*, 51(2):6500704, 2015. doi:10.1109/TMAG.2014.2335536.

[8] Y. Toshida, K. Enpuku, J. Dieckhoff, M. Schilling, and F. Ludwig. Magnetic fluid dynamics in a rotating field. *J. Appl. Phys.*, 111(5):053901, 2012. doi:10.1063/1.3688254.

[9] D. Knuth. *The Art of Computer Programming Vol. 2: Seminumerical Algorithms*. Addison-Wesley Longman, Reading, 1998.